

A Monolithic 2k x 2k LWIR HgCdTe Detector Array for Passively Cooled Space Missions

Meghan Dorn^a, Craig McMurtry^a, Judith Pipher^a, William Forrest^a, Mario Cabrera^a, Andre Wong^b, A. K. Mainzer^b, Donald Lee^c, and Jianmei Pan^c

^aUniversity of Rochester, Rochester, NY 14627 (USA)

^bJet Propulsion Laboratory, California Institute of Technology, Pasadena, CA 91102 (USA)

^cTeledyne Imaging Sensors, Camarillo, CA 93012 (USA)

ABSTRACT

A 2K x 2K 10 μm cutoff HgCdTe array for background-limited space astronomy has been developed by Teledyne Imaging Sensors to specifications set by JPL, and demonstrated by University of Rochester at a focal plane temperature of 40K for the proposed JPL Near-Earth Object Camera (NEOCam) survey mission under the NASA Planetary Defense Coordination Office. We describe the detector performance for the first large format monolithic HgCdTe detector array tested, including the dark current, well depth, dark current vs. temperature, quantum efficiency, latent image performance, and read noise.

Keywords: HgCdTe, LWIR, NEOCam, infrared detector, space telescope, astronomy

1. INTRODUCTION

The Near-Earth Object Camera (NEOCam) is a proposed NASA Planetary Defense Coordination Office survey mission whose goal is to detect most asteroids and comets ≥ 140 m in diameter that may pose a threat to the Earth, i.e. near-Earth objects (NEOs).^{1,2} NEOCam was one of five proposals selected for the Step 2 phase of the Discovery program competition in September, 2015, and in 2017 was awarded Extended Phase A funding under the NASA Planetary Defense Coordination Office. The telescope requires two channels; in the original Step 1 phase of the Discovery competition, we proposed sixteen 1024 x 1024 long-wave IR (LWIR) HgCdTe detector arrays sensitive from 6-10 μm , and another with four mid-wave IR (MWIR) 2048 x 2048 arrays sensitive from 3-5 μm with the same design as the MWIR detector arrays for JWST. University of Rochester (UR) and NASA JPL have been working with Teledyne Imaging Sensors (TIS) to develop and demonstrate the performance of the LWIR HgCdTe arrays.³ At the time NEOCam was selected for Step 2, TIS began development of 2048 x 2048 pixel LWIR arrays. Increasing the array format results in fewer and smaller gaps between individual arrays, and reduced complexity of packaging, electronics, and cabling. At the time of Extended Phase A, TIS had only developed an array referred to as a ‘duplex’ detector: two 1k x 2k (952 x 2048 pixels) arrays bump bonded to the same H2RG read-out with a gap in the middle as small as practicable.⁴ Since then, TIS has produced and delivered 3 monolithic (i.e. fabricated from one single continuous die) 2k x 2k arrays to UR. We report here the performance of one of those arrays; the other two were bonded to engineering-grade multiplexers that were revealed to have sub-par performance when tested, due to the engineering-grade multiplexer.

The nominal 10 μm cutoff wavelength detectors are fabricated using $\text{Hg}_{1-x}\text{Cd}_x\text{Te}$ (mercury-cadmium-telluride), a ternary compound comprised of 50% tellurium and 50% a mixture of mercury and cadmium. By changing the ratio of mercury to cadmium by varying x , the mole fraction of cadmium, the bandgap energy, and therefore cutoff wavelength can be tuned to the desired value. The cutoff wavelength can vary from 0.7 to 25 μm .⁵ For the nominal NEOCam focal plane temperature ($T=40$ K) and $x=0.232$, a cutoff wavelength of 10 μm is achieved. The arrays are fabricated via epitaxial growth by MBE on an 800 μm thick CdZnTe substrate material lattice matched to the HgCdTe detector material. Each pixel is bump bonded to a H2RG read-out integrated circuit (ROIC). After hybridization, each detector array is substrate thinned with ~ 30 μm CdZnTe remaining. With a full substrate, the cuton wavelength is 0.8 μm , and a fully substrate removed detector array can have a cuton wavelength into the UV-Visible.

2. ARRAY CALIBRATION

The detector array described in this paper, SCA H2RG-18694, was tested at a focal plane temperature of 40 K, the nominal focal plane temperature for NEOCam to maintain the dark current requirement of $200 \text{ e}^-/\text{s}$, and an applied bias of 250 mV, ideal to achieve the required well depth of $>44,000 \text{ e}^-$. All tests were performed at 40 K, with the exception of the experiment to determine dark current vs. temperature. See Table 1 for NEOCam requirements.

The UR test system includes a liquid helium dewar containing a ZnSe window followed by a filter wheel cooled to 4 K. The filter wheel contains a cold dark slide that is used for dark current and read noise measurements, as well as several filters. Light from external sources passes through a $67.6 \mu\text{m}$ diameter Lyot stop that is located 40.5 mm from the surface of the array. For previously tested $1\text{k} \times 1\text{k}$ arrays, the flood illumination pattern at a distance of 43.8 mm away from the Lyot stop aperture filled the array. Since the $2\text{k} \times 2\text{k}$ arrays described in this paper sit closer to the Lyot stop, the tests performed utilizing light through the filter wheel produced a circular pattern that does not illuminate the extreme corners of the array. For this reason we only examine the quantum efficiency and linearity for pixels within the illuminated region. Uniformity across the illuminated region is not required to saturate pixels when determining the well depth. The UR test system is described in detail in McMurtry et al. (2013) and Forrest et al. (1985), as is the method of calibration, described below.^{3,6}

When an image is read out by our electronic system, the signal passes through two amplification FETs in the output path of the ROIC.⁷ The source follower FET gain is first measured by varying the reset voltage with the reset switch on and observing the change in output voltage. We then measure the nodal capacitance per pixel, which gives us the conversion from output voltage to electrons. This measurement is required to calibrate read noise, dark current, well depth, and quantum efficiency data, and is determined using the signal vs. noise squared method⁸ from a series of images obtained with varying source flux and integration time, capturing the signal and the noise for low to higher signals. The capacitance per pixel is over estimated by a small amount due to nearest neighbor crosstalk, so it is corrected for interpixel capacitance (IPC).⁹ The total percentage of IPC measured for this array is 8.8% from a pixel to its nearest neighbors.

When the detector array is illuminated it debiases, and the nodal capacitance changes as we integrate charge, leading to a non-linear response. To calibrate the non-linearity, we illuminate the detector array with a constant but relatively low flux and obtain images at successively longer integration times. For our non-linear photovoltaic detectors, we plot the normalized flux as a function of fluence, and determine the line that intersects unity at zero fluence, the slope of which is the correction factor for our images at a specific fluence. (Diodes that are perfectly linear would show a flat line at unity with no slope.)

Images are read out in two modes: either sampled up-the-ramp (SUTR), or as a correlated double sampled (CDS) image. In SUTR mode, the array is reset, then multiple image frames are read non-destructively with a set amount of time between frames. A CDS image is the difference of two consecutive images taken after reset and during the same integration ramp. Differencing the two images removes kTC noise from the transfer of charge on the integrating node following reset.

Table 1. Minimum NEOCam Requirements for LWIR focal plane and Detector Array Characteristics

	NEOCam Requirement	H2RG-18694
Detector Material	HgCdTe; CdZnTe substrate thinned	HgCdTe; CdZnTe substrate thinned
Array Format	2048x2048 Duplex	2048x2048 Monolithic
Cutoff Wavelength	>10	9.6
Responsive Quantum Efficiency (%)	>55	71
CDS read noise (e^-)	<36	19
Dark Current (e^-/s)	<200	<200*
Well Depth (e^-)	>44,000	>44,000*
Operability (%)	>90	98.9

* The median dark current for this array is $0.3 e^-/s$ /pixel and the median well depth is $65,000 e^-$

3. DARK CURRENT AND WELL DEPTH

Dark current and well depth measurements are obtained by monitoring in the detector array SUTR mode as it integrates in the dark. After some time, the detector is exposed to $8.6 \mu m$ radiation in order to saturate all the pixels. The difference between the saturation level and the first read is the well depth, and the slope of the signal vs. time in the dark before moving the filter wheel is the dark current. Plotting the two values against each other provides a diagnostic tool to determine the cause of bad pixels. In the past we have seen pixels limited by their dark current, well depth, or a combination of the two.^{10,11}

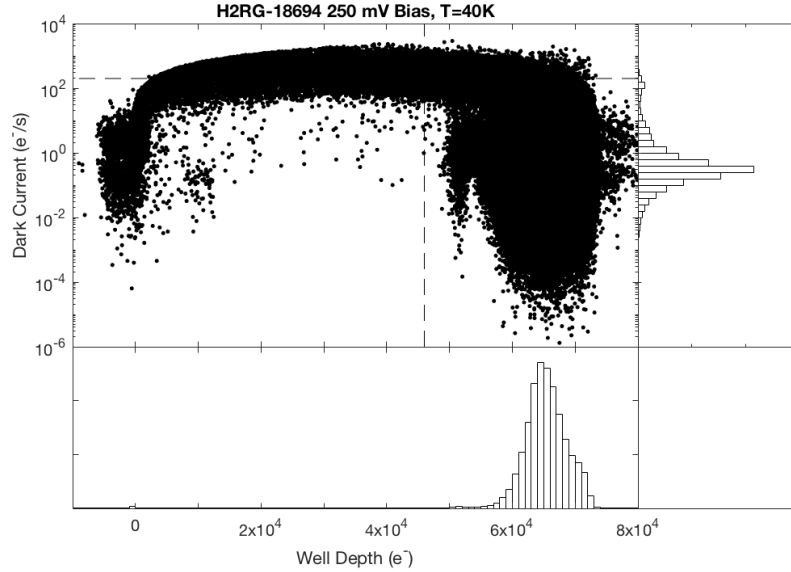


Figure 1. Dark current vs. well depth for infrared active pixels for H2RG-18694. Data obtained at $T=40 K$ and an applied bias of 250 mV. The dark current and well depth requirements for NEOCam are illustrated graphically.

Figure 1 shows the dark current vs. well depth of the infrared active pixels for H2RG-18694. The histograms on the x- and y- axes show that the median dark current for this array is $0.3 e^-/s$ and the median well depth is $65,000 e^-$. Although there appears to be a large scatter in the well depth and dark current, 98.9 % of pixels have dark current $<200 e^-/s$ and well depth $>44,000 e^-$, well exceeding the NEOCam requirement. Pixels with

apparently low dark current, but small well depth are high dark current pixels which have debiased substantially before the first read. For pixels that meet the well depth requirement, 90% of pixels have a dark current <3 e^-/s (Figure 2).

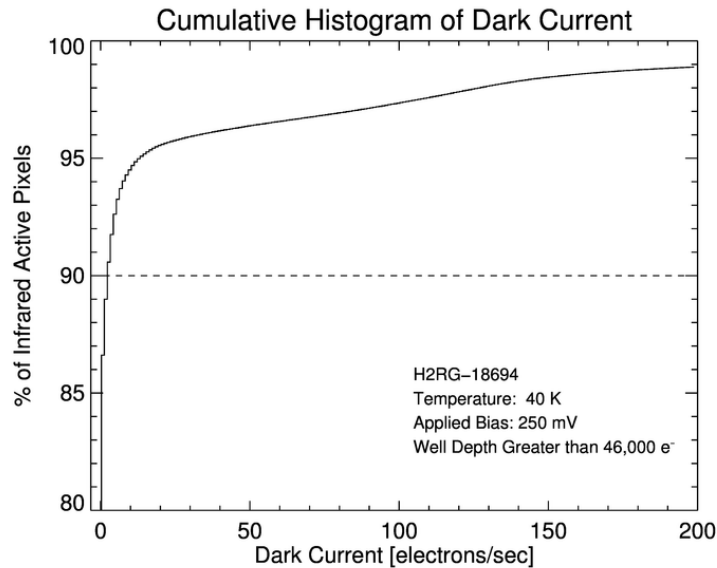


Figure 2. Cumulative histogram of dark current for pixels with well depth $>44,000$ e^- for H2RG-18694. Data obtained at $T=40$ K and an applied bias of 250 mV.

4. DARK CURRENT VS. TEMPERATURE

There are two sources of thermal dark current. The first, diffusion current, is from random thermal generation and recombination of electron-hole pairs in the bulk detector material. If the electron-hole pair is generated within a minority carrier diffusion length of the depletion region, the charge will be integrated at the diode. The other thermal mechanism, generation-recombination (g-r) current, arises from traps located within the depletion region assisting a thermally generated electron-hole pair. One of the charges will be trapped, and if the lifetime is longer than the integration time, the other charge will not recombine and therefore be read out. Operating these detectors at low temperatures reduces the effect of the inherent thermal dark current components, but as the temperature is reduced, other sources of dark current begin to dominate.

Detectors with a small bandgap, as are presented here, are dominated by tunneling current at low temperatures. Charges can either tunnel directly across the bandgap, or tunnel across the bandgap with the assistance of a trap with energy between the conduction band and valence band energy levels. Dark current tunneling mechanisms are strongly dependent on the applied reverse bias. We do not find evidence of significant detectable direct band-to-band tunneling in our modeling, although there may be some rate of band-to-band tunneling below the detection limit for the measurement system.

The total dark current is the sum of all contributing dark current mechanisms. We identify sources of dark current by examining the dark current as a function of temperature and as a function of reverse bias per pixel. We obtain dark current data while the detector is held at three stable temperatures: $T=35$, 40, and 42 K, and at each temperature, with three applied reverse biases: $V=150$, 250, 350 mV. In order to analyze the dark current at higher temperatures, we take fast (0.2 s) subarray reads as the dewar warms up.

From the 42,920 pixels in the subarray that meet the NEOCam dark current operability requirement (at 40 K, 250 mV reverse bias), two distinct groups of pixels were identified. The first group, representing 3/4 of the pixels, show some trap-to-band tunneling current at low temperatures. Figure 3 shows an average Arrhenius plot of dark current vs. inverse temperature for this group of pixels. These pixels are dominated at higher temperatures by

diffusion current, down to ~ 43 K. Between 43-41 K, the dark current is dominated by generation recombination (g-r) current. At 41 K, the dark current reaches a near constant level attributed to a light leak of ~ 0.2 e^-/s in our dewar that has been previously observed by our group.³ Evidence of trap-to-band tunneling current can be seen in the right-most two data points in the left figure in Figure 3, where the dark current increases slightly as the temperature is decreased from 40 K to 35 K. Trap to band tunneling has a weak dependence on temperature, but a very strong dependence on bias. As we increase the negative applied bias, we observe an exponential increase in the dark current above the light leak level.

The remaining 1/4 of the pixels are dominated by diffusion current down to ~ 42 K. Between ~ 42 - 41 K, there is a more significant contribution of g-r current. Below 41 K, these pixels have a constant dark current as a function of temperature and applied bias and therefore do not show appreciable tunneling current that can be detected above the light leak. An averaged Arrhenius plot for this group of pixels is shown in the right figure in Figure 3.

McMurtry et al. (2013) show that the previous generation of 1K x 1K detector arrays were limited by g-r current between ~ 42 K and 37 K, and below 37 K the detectors are limited by the very small light leak in our dewar. The most recent generation of 2K x 2K pixel arrays are also limited by g-r current at ~ 42 K, but reach the light leak limit at 40 K. G-r current becomes the dominating current that contributes to the total current at different temperatures, because there is a difference in cutoff wavelength for the detectors reported. The cutoff wavelength measured for detector array H2RG-18694 is 9.6 μm , whereas the detector array that was reported by McMurtry et al. has a cutoff wavelength of 10.6 μm . The longer wavelength cutoff detector has a smaller bandgap, and therefore will have larger thermal dark current than a similar device with larger bandgap at the same temperature.

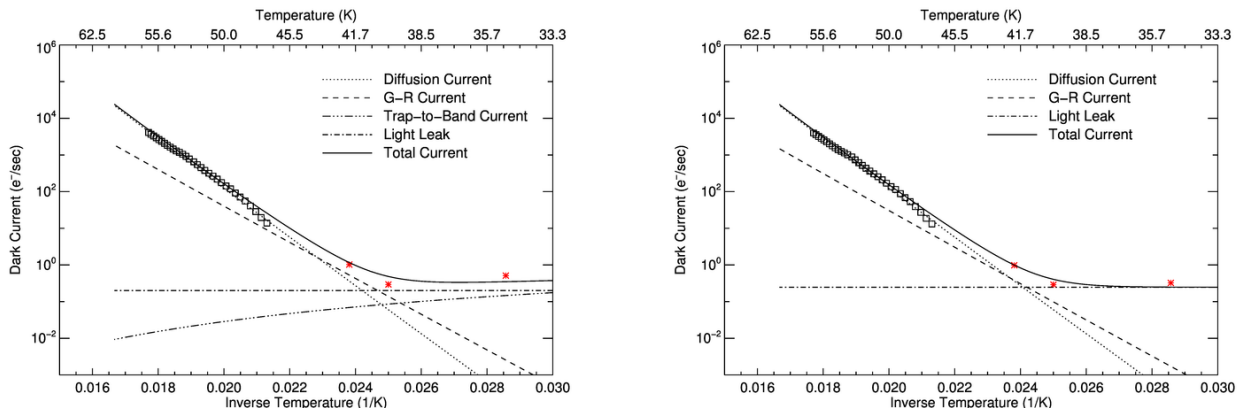


Figure 3. Left: Arrhenius plot for pixels that have some tunneling current, Right: Arrhenius plot for pixels with no tunneling current. The applied bias for these data is 250 mV. Red data point represent the data obtained while the detector was at a constant temperature, and black data points represent the data from the fast subarray reads while the detector warmed up.

5. READ NOISE AND QUANTUM EFFICIENCY

The CDS read noise is calculated by computing the standard deviation of each pixel from 64 CDS images. The median CDS read noise is 19 e^- , and 93% of pixels have a read noise < 36 e^- . Pixels with higher read noise are randomly distributed spatially across the array.

The responsive quantum efficiency measured for this array is 71% between 8-9 μm , exceeding the NEOCam requirement of 55% with no anti-reflection coating. TIS measured 74% QE at 9 μm on a process evaluation chip (PEC) at T=30 K. The cutoff wavelength for this array is 9.6 μm , slightly lower than the desired cutoff wavelength (10 ± 0.3 μm). Higher QE will be achieved with an anti-reflection coating.

6. IMAGE LATENCY

A series of tests were designed to probe the image latency when a detector is flood illuminated by both lower and higher flux sources. Trapping and recombination centers induced by the presence of impurities and lattice defects can create latent images that persist after the signal from an illuminating source has been read and the array has been reset. Latent images produced by bright sources can potentially serve as a source of spurious detections that can confound efforts to link detections of moving solar system objects.

The long-wave NEOCam camera will take 8 observations with an integration time of 3 s with a total on-source time of 28 s (including overhead), followed by a 2 s slew for the dither. The first test performed was with a source flux that is close to the minimum background/maximum dark current for NEOCam. The source, a room temperature blackbody, was viewed through a 10.25 μm filter for 28 s (the longest time a source will be on the detector). The second test was performed with the same integration time, but with a much higher flux, in order to saturate the array. The third test is a variation of the first test - the detector is exposed for 3 s, a more NEOCam-like integration time, to a non-saturating source flux. The filter used here was the L' filter (centered at 3.75 μm , with a bandwidth of 0.807 μm) a higher flux than in the first test in order to reach $\sim 1/5$ the well depth in 3 s. The fourth test is a variation on the second test, exposed to a saturating flux, but saturated in 3 s, rather than 28 s. Finally, the fifth test was a saturating flux exposed for >1 hour, followed by a 2 s delay, and 3 s dark exposures. This test is performed in order to simulate a bright source in the field of view of the detector while data are downlinked. The wavelength of the filter chosen for each test was selected to achieve a desired fluence on the array, not because the wavelength itself was significant. Table 2 summarizes the test design.

Table 2. Residual image test design.

Test	Wavelength (μm)	Source Flux (e^-/s)	Source Exposure (s)	Source Fluence (e^-)	Delay (s)	Dark Exposure (s)	Desired Residual Fluence (e^-)
1	10.25	200	28	5,600	8	28	<100
2	8.6	$>2,500$	28	$>70,000$	10	28	<200
3	3.75	3,000	3	9,000	6	3	<100
4	8.6	$>20,000$	3	$>60,000$	10	3	<200
5	8.8	$>20,000$	3,600	$>60,000$	3	3	<200

For each test, the detector was exposed to the source fluence listed in column 4 for the amount of time shown in column 3, followed by a delay as the filter wheel moved back to the cold dark slide, then a series of 50 dark exposures integrated for the amount of time shown in column 6. Between each test, there is a wait time of 10 min. Although the tests were designed to simulate the NEOCam slew, the time it takes to move from a filter to the cold dark slide can be much longer (up to 10 s). One of the filters, 8.8 μm , is very close to the cold dark slide, but did not saturate the array in 28 s, so could only be used for the final test, when the detector is illuminated for one hour.

In order to analyze these data, a box of pixels within a saturated region of the array was selected by looking at the pattern of illumination from the tests that saturated the array. Then, the signal measured in dark images obtained after illumination was extracted from the same region of the array. The dark charge measured before these tests was subtracted from each image and pixels that were previously identified as inoperable were excluded from the analysis.

Tests 1 and 3 both exposed the detector array to non-saturating flood illumination for 28 s and 3 s respectively. The first dark frame was obtained ~ 10 s after reset, and no residual flux was detected for either array within measurement uncertainty.

After the detector was exposed to saturating illumination for 28 s, there appeared to be some residual flux (Figure 4). The $3.4 \pm 2 \text{ e}^-/\text{s}$ flux measured in the first frame in the dark after illumination is one order of magnitude greater than the $0.3 \pm 0.1 \text{ e}^-/\text{s}$ dark current measured before testing, but two orders of magnitude

lower than the NEOCam dark current requirement. The pixels settle to the noise level of the measurement by the 2nd dark image.

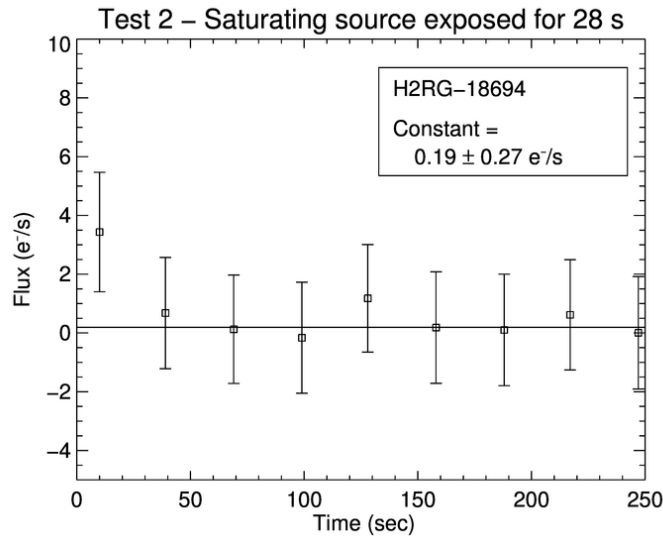


Figure 4. CDS dark current vs. time after the detector was illuminated for 28 s

For test 4, the detector was exposed to the same source as test 2, but in this case, the detector was illuminated for 3 s. The $\sim 14 e^-/s$ residual flux detected is above the dark current measured before these tests (Figure 5). In comparison, when the amount of time a saturating source is on the detector is increased to 1 hr (test 5), the residual flux in the first dark frame, $\sim 15 e^-/s$ (Figure 6).

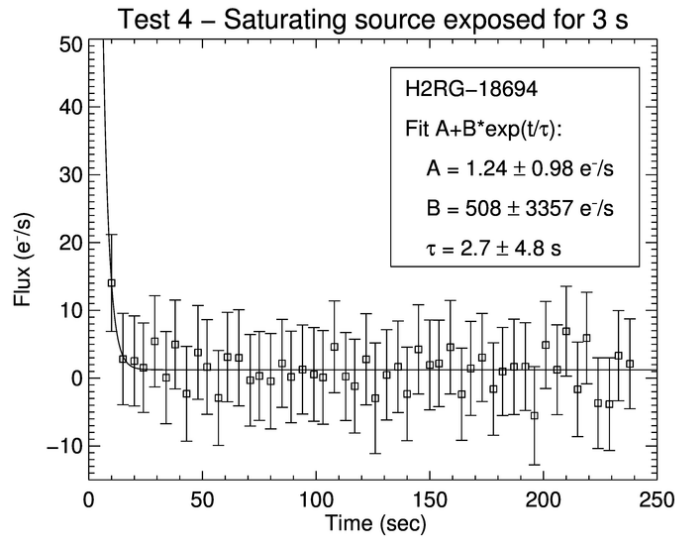


Figure 5. CDS dark current vs. time after the detector was illuminated for 3 s.

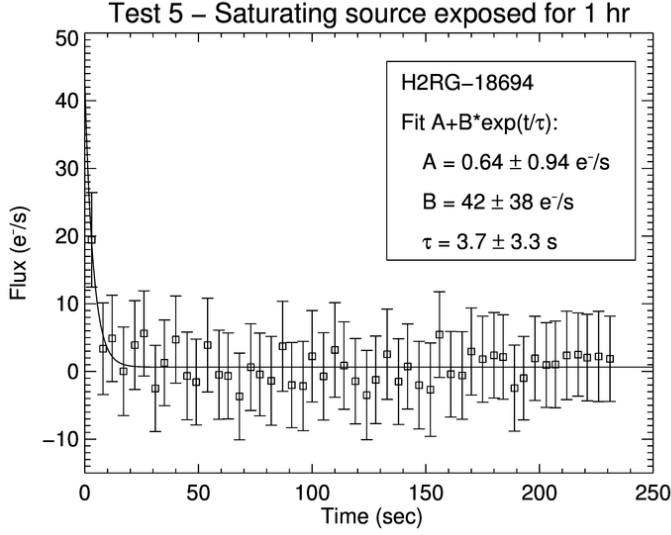


Figure 6. CDS dark current vs. time after the detector was illuminated for 1 hr.

The expression $F = A + B \exp(-t/\tau)$ was fit to the flux vs. time following illumination for tests 4 and 5 where there is more data to fit immediately following the illumination. The decay constant, τ , gives the trap lifetime for the residual flux, and the constant, A , is the asymptotic level to which the detector decayed. The trap lifetimes are listed in Table 3. Although the uncertainty is high, this experiment has been reproduced with a different NEOCam array (H1RG-17346) and verified to be 1.6 ± 0.8 s, but with the same experiment repeated multiple times. That result is also listed.

Table 3. Trap lifetimes obtained from fitting the expression $F = A + B \exp(-t/\tau)$ to the flux vs. time and measured residual fluence (c.f. Table 2)

Test	H2RG-18694 Trap Lifetime (s)	H1RG-17346 Trap Lifetime (s)	Measured Residual Fluence (e^-)
2	no fit - sparse data	1.5 ± 0.6	< 200
4	2.7 ± 4.8	1.7 ± 0.7	< 200
5	3.7 ± 3.3	1.4 ± 0.6	< 200

7. SUMMARY

We demonstrated the performance for a monolithic LWIR 2k x 2k pixel detector array intended for the proposed survey mission NEOCam. This detector array has a well depth and dark current operability of 98.9%, exceeding the NEOCam requirement of 90%, and meets the NEOCam requirements for quantum efficiency and read noise.

By fitting dark current mechanisms to dark current vs. temperature Arrhenius plots, we demonstrate that the dark current measured for the majority of pixels is dominated by the $\sim 0.2 e^-/s$ light leak in the dewar at 40 K, the nominal NEOCam focal plane temperature.

Various tests were carried out to measure possible image latency from an illuminating source for situations that may be encountered by the NEOCam survey design. For non-saturating illumination, there is no detectable residual flux. The maximum residual flux detected, $\sim 15 e^-/s$, was present when a saturating source was on the detector for one hour and is an order of magnitude below the dark current requirement for NEOCam. Any residual flux detected decayed to the noise level by the second image taken in the dark after illumination.

ACKNOWLEDGMENTS

This research was carried out at the University of Rochester and the Jet Propulsion Laboratory, California Institute of Technology, under a contract with the National Aeronautics and Space Administration.

The information presented about NEOCam is pre-decisional and is provided for planning and discussion purposes only.

REFERENCES

- [1] Mainzer, A. K., Grav, T., Bauer, J., Conrow, T., Cutri, R. M., Dailey, J., Fowler, J., Giorgini, J., Jarrett, T., Masiero, J., Spahr, T., Statler, T., and Wright, E. L., “Survey simulations of a new near-Earth asteroid detection system,” *The Astronomical Journal* **149**(5), 172 (2015).
- [2] Grav, T., Mainzer, A. K., and Spahr, T., “Modeling the performance of the LSST in surveying the near-Earth object population,” *The Astronomical Journal* **151**(6), 172 (2016).
- [3] McMurtry, C. W., Lee, D., Beletic, J., Chen, C. A., Demers, R. T., Dorn, M., Edwall, D., Fazar, C. B., Forrest, W. J., Liu, F., Mainzer, A. K., Pipher, J. L., and Yulius, A., “Development of sensitive long-wave infrared detector arrays for passively cooled space missions,” *Optical Engineering* **52**(9), 091804–091804 (2013).
- [4] McMurtry, C. W., Dorn, M., Cabrera, M. S., Pipher, J. L., Forrest, W. J., Mainzer, A. K., and Wong, A., “Candidate 10 micron HgCdTe arrays for the NEOCam space mission,” in [*High Energy, Optical, and Infrared Detectors for Astronomy VII*], *Proc. SPIE*, 99150D–99150D (2016).
- [5] Norton, P., “HgCdTe infrared detectors,” *Opto-electronics Review* **10**(3), 159–174 (2002).
- [6] Forrest, W. J., Moneti, A., Woodward, C. E., Pipher, J. L., and Hoffman, A., “The new near-infrared array camera at the University of Rochester,” *Publications of the Astronomical Society of the Pacific* **97**(588), 183 (1985).
- [7] Blank, R., Anglin, S., Beletic, J. W., Bhargava, S., Bradley, R., Cabelli, C. A., Chen, J., Cooper, D., Demers, R., Eads, M., Farris, M., Lavelle, W., Luppino, G., Moore, E., Piquette, E., Ricardo, R., Xu, M., and Zandian, M., “H2rg focal plane array and camera performance update,” in [*High Energy, Optical, and Infrared Detectors for Astronomy V*], *Proc. SPIE* **8453**, 845310 (2012).
- [8] Mortara, L. and Fowler, A., “Evaluations of CCD: Performance for Astronomical Use,” in [*Proc. SPIE, Solid State Imagers for Astronomy*], **290**, 28–30 (1981).
- [9] Moore, A. C., Ninkov, Z., and Forrest, W. J., “Interpixel capacitance in nondestructive focal plane arrays,” in [*Proc. SPIE, Focal Plane Arrays for Space Telescopes*], Grycewicz, T. J. and McCreight, C. R., eds., **5167**, 204–215 (Jan. 2004).
- [10] Bacon, C., Pipher, J. L., Forrest, W. J., McMurtry, C. W., and Garnett, J. D., “Diode characterization of rockwell lwir hgcdte detector arrays,” in [*IR Space Telescopes and Instruments*], *Proc. SPIE* **4850** (2003).
- [11] Bacon, C., McMurtry, C. W., Pipher, J. L., Mainzer, A. K., and Forrest, W. J., “Effect of dislocations on dark current in lwir hgcdte photodiodes,” in [*High Energy, Optical, and Infrared Detectors for Astronomy IV*], *Proc. SPIE* **7742**, 77421U (2010).